

# Radar Cross-Section Characterization of the Car In-Cabin Environment at Sub-THz Frequencies

Victor Pettersson<sup>#1</sup>, Sining An<sup>\*2</sup>

<sup>#</sup>Veoneer Research, Veoneer Sweden AB, Vårgårda, Sweden

<sup>\*</sup>Department of Microtechnology and Nanoscience, Chalmers University of Technology, Gothenburg, Sweden

<sup>1</sup> victor.pettersson@veoneer.com, <sup>2</sup> sininga@chalmers.se

**Abstract**— Radar sensors at sub-THz frequencies (100 - 330 GHz) can potentially be used in car in-cabin monitoring systems. In designing such sensors, knowledge of the in-cabin propagation conditions at the sub-THz bands is useful. Considering the rather novel use-case, such data is not readily available and must be gathered through measurements. This paper presents a Radar Cross-Section (RCS) imaging system, which has been developed in order to characterize the reflective properties of common car in-cabin objects at 243 GHz. The system produces two types of data, RCS profiles and Inverse Synthetic Aperture Radar (ISAR) images, which can be analyzed jointly to give an intuitive and detailed view of object reflectivity. The system applies range-domain processing and prove efficient in ignoring peripheral reflection points and multipath, which allows for conducting compact measurements in an enclosed lab environment. The ISAR images achieve 1-2 centimeter spatial resolution, and thus demonstrates the fine-resolution capabilities of sub-THz radar systems.

**Keywords**— In-cabin, sensing, driver monitoring, radar, radar cross-section, imaging, sub-THz, THz, terahertz.

## I. INTRODUCTION

In-cabin monitoring is a key enabler in assuring passenger safety of modern cars. Such systems aim to infer passengers' seating position and health status and relay the information to the driver or a central controller. The sub-THz frequency range (100 - 330 GHz) could potentially allow for very compact, non-intrusive in-cabin sensing solutions while at the same time promising high spatial resolution.

A car in-cabin radar operates in an enclosed propagation environment and the received waveform will be the superposition of many direct reflections and multipath. The system described in this paper examines the reflective properties of individual in-cabin objects and humans in order to better understand the in-cabin propagation environment at sub-THz frequencies. More specifically, the *Radar Cross-Section* (RCS) of in-cabin objects and humans is examined at 243 GHz. Only a few examples of previous similar measurement campaigns could be found: [1] for example, where the RCS of a mannequin is measured for 220 GHz.

### A. Radar Cross-Section

In radar systems, the received power is a function of target reflectivity. And the reflective property of an object is usually quantified using the RCS, commonly denoted  $\sigma$ , which is an equivalent area that relates the backscattered power to the incident power density [2]. Assuming a monochromatic

waveform of frequency  $f$ , the RCS manifests itself in the received complex electric field as the integral:

$$E(f) \propto \iiint_{\mathcal{I}} \sqrt{\sigma(x, y, z)} e^{-j2\pi f \ell(x, y, z)/c} dx dy dz \quad (1)$$

according to [3], where  $\ell(x, y, z)$  is the total path length traveled by the waveform,  $c$  is the speed of light in a vacuum and  $\sqrt{\sigma(x, y, z)}$  is the square-root RCS distribution per unit volume. The region  $\mathcal{I}$  contains all reflection points of the object which are currently illuminated by the radar.

## II. MEASUREMENT SETUP

### A. Data Acquisition

This paper presents two different methods of analyzing object reflectivity, but the measurement setup and geometry is identical in both cases and is shown in Fig. 1a. The image shows a bistatic radar arrangement, realized by two horn antennas connected via two frequency extender modules to a vector network analyzer (VNA). The radar observes a target placed on a rotating table, and the frequency response of the resulting two-port is sampled at  $N$  linearly increasing, uniformly spaced frequency points within a 10 GHz bandwidth with center frequency  $f_c = 243$  GHz. A number of such measurements, referred to as *frequency sweeps*, are made at regular intervals of target rotation, and the coordination is handled by VNA-control software on a PC connected via USB.

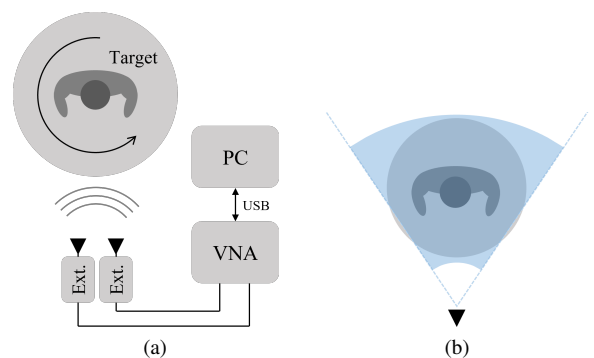


Fig. 1. (a): Measurement setup. (b): Illustration of range-gating concept.

### B. Hardware

The VNA used is a Keysight N5242A PNA-X Microwave Network Analyzer that works up to 26.5 GHz. The extenders

are VDI model WR3.4-VNAX which works from 220 to 330 GHz. Antennas are ERAVANT WR-03 pyramidal horn antennas with an operating range of 220 to 325 GHz and a specified nominal gain of 25 dBi corresponding to an approximate  $10^\circ$  3 dB-beamwidth in both E- and H-planes.

Theoretically, a single-port measurement with one extender could detect the reflected signal (monostatic radar). However, an internal reflection with this configuration was observed, and it was too strong compared to any external reflection due to the considerable path loss of the sub-THz signal. Instead, two extenders are used and two-port measurements are made.

### C. Amplitude Calibration

The VNA is first calibrated at the reference plane of the extender wave guide flanges, but the signal amplitude must still be calibrated against uncertainties in the radar two-way antenna gain  $G^2$ . The gain is assumed constant over the scope of the rotating table. This assumption is reasonable if the table is placed far away enough so that the target is contained in the 3 dB-beamwidth entirely. The gain is calibrated against a reference target of known RCS, which is a metallic sphere of diameter  $D = 30$  cm with  $\sigma_{\text{sphere}} = \pi D^2/4 \approx 0.071 \text{ m}^2$  for  $D/2 \gg \lambda$ , where  $\lambda$  is the signal wavelength [4]. Let  $G_{\text{uncal}}^2$  denote the two-way uncalibrated gain, then calibration is performed by

$$G^2 = G_{\text{uncal}}^2 \frac{\sigma_{\text{app.}}}{\sigma_{\text{sphere}}} \quad (2)$$

similar to what is described in [2] and  $\sigma_{\text{app.}}$  is the apparent RCS of the sphere from a measurement.

## III. ANALYZING TARGET REFLECTIVITY

As described in section II-A, the radar measures the frequency response of the transmitter-to-target-to-receiver two-port network. More specifically, the received data are samples of the complex S21-parameter denoted  $S_{21}(f)$ . The following subsections presents two analysis methods of target reflectivity based on such data.

### A. RCS Profiles

An estimate of the target RCS is produced by measuring the received-to-transmitted power ratio, denoted  $|S_{21}(f, \theta)|^2$ , at different target viewing angles  $\theta$ . The estimate is

$$\hat{\sigma}(f, \theta) = \frac{(4\pi)^3 R^4}{G^2 \lambda_c^2} |S_{21}(f, \theta)|^2 \quad (3)$$

using (1.19) in [2] and assuming no additional losses apart from free space loss. The range  $R$  is taken as the distance from the radar to the rotating table center and  $\lambda_c$  is the sweep center wavelength.

The measured RCS in (3) can be interpreted as estimating the magnitude square of the integral in (1), where the illuminated region  $\mathcal{I}$  is varied with the different viewing angles. Peripheral scatterers and multipath reflections are partly ignored via the antenna beam, and partly by using *range gating*. The latter is performed digitally, where  $N$ -point complex S21 data is inverse Fourier transformed and brought

into the range domain. Energy from range bins outside the extent of the rotating table is filtered out, and the data is then brought back into the frequency domain. The region  $\mathcal{I}$  is therefore constrained within only a part of the antenna beam, as indicated by the shaded area illustrated in Fig. 1b.

### B. ISAR Imaging

With *Inverse Synthetic Aperture Radar* (ISAR) imaging, the aim is to create an image of the *spatial RCS distribution*  $\sigma(x, y, z)$  presented in (1). The region  $\mathcal{I}$  is now partitioned into small volume elements and estimates of their individual contributions are made [3]. Here, images assume a 2D geometry and the spatial RCS distribution is thus  $\sigma(x, y)$  and can be thought of as a top-down, cross-sectional view of the target.

#### 1) Data Model

Imagine a single reflection point, characterized by its 2D coordinates  $(x_p, y_p)$  and RCS per unit volume  $\sigma_p$ , that is located in free space and is observed by one transmitting and receiving antenna located at positions  $\vec{a}_{\text{tx}}$  and  $\vec{a}_{\text{rx}}$ , respectively. The waveform travels a total length of

$$\begin{aligned} \ell(x_p, y_p) &= R_{\text{tx}}(x_p, y_p) + R_{\text{rx}}(x_p, y_p) \\ &= \|(x_p, y_p) - \vec{a}_{\text{tx}}\| + \|\vec{a}_{\text{rx}} - (x_p, y_p)\| \end{aligned} \quad (4)$$

and the measured  $S_{21}(f)$  will become

$$S_{21}(f, x_p, y_p) = \alpha(x_p, y_p) e^{-j2\pi f \ell(x_p, y_p)/c} \quad (5)$$

where

$$\alpha(x_p, y_p) = \sqrt{\frac{G^2 \lambda_c^2 \sigma_p}{(4\pi)^3 R_{\text{tx}}^2(x_p, y_p) R_{\text{rx}}^2(x_p, y_p)}} \quad (6)$$

is the magnitude response of the two-port, similar to (6.11) in [3].

#### 2) Overview of Image Reconstruction Algorithm

First, a grid of pixels with coordinates  $(x, y)$  is defined that covers the area in which  $\sigma(x, y)$  is estimated, and the pixel values are zero-initiated. As described in section II-A,  $S_{21}(f)$ -sweeps are collected at a number of viewing angles. The  $M$  sweeps are numbered  $m = 0, 1, \dots, M-1$  and the regularly spaced viewing angles become  $\theta_m = m\Delta\theta$ , where  $\Delta\theta$  is the viewing-angle spacing. Range compression of the  $m$ :th sweep is performed using an inverse Fourier transform:

$$s_{21}^{(m)}(\ell') = \mathcal{F}^{-1} \left\{ S_{21}^{(m)}(f) \right\}. \quad (7)$$

Then, for each  $s_{21}^{(m)}(\ell')$  the following steps are performed:

- 1) Relative positions of antennas and pixels are calculated using the current viewing angle  $\theta_m$  and knowledge of the measurement geometry in Fig. 1a. Note that the current transmitter-to-pixel-to-receiver distance  $\ell(x, y, \theta_m)$  becomes a function of  $\theta_m$ .
- 2) For each set of pixel coordinates the compressed data is queried at points  $s_{21}^{(m)}(\ell' = \ell(x, y, \theta_m))$  and

pixel-variant factors in (5) are compensated by multiplication with

$$\begin{aligned} \mathcal{C}(x, y, \theta_m) &= \\ &= R_{\text{tx}}(x, y, \theta_m) R_{\text{rx}}(x, y, \theta_m) e^{j2\pi f_c \ell(x, y, \theta_m)/c}. \end{aligned} \quad (8)$$

The resulting product is added to the corresponding pixel value.

The coherent summation over multiple viewing angles results in an image of the square-root RCS distribution. Including proper scaling, the image expression  $I(x, y)$  becomes

$$\begin{aligned} I(x, y) &= \\ &= \frac{(4\pi)^{3/2}}{G\lambda_c} \left( \frac{1}{M} \sum_{m=0}^{M-1} s_{21}^{(m)}(\ell(x, y, \theta_m)) \mathcal{C}(x, y, \theta_m) \right). \end{aligned} \quad (9)$$

The image can be seen as an estimate of the target spatial square-root RCS distribution, but this is only true for small collection angles. The described procedure is a process usually referred to as *back-projection* in radar literature, and it focuses the backscattered energy of a reflection point onto its respective coordinates in the image. A similar algorithm is described in [5], where it is referred to as the standard back-projection algorithm.

Also, to ensure good image quality, *aliasing* must be avoided, which would appear as strange artifacts in the image. Aliasing is prevented by choosing the angular spacing  $\Delta\theta$  according to

$$\Delta\theta \leq \frac{\lambda_c}{2D_{\text{min}}} \quad (10)$$

where  $D_{\text{min}}$  is the minimum diameter of a circle which entirely contains the target to be imaged, and is centered at the axis of rotation [6].

#### IV. RESULTS AND DISCUSSION

Data collection efforts were performed using  $N = 401$  point sweeps at a repetition rate of ten times per second (1/100 ms) while the table was rotating at an assumed constant speed. The distance from the radar to the table center was usually around 2 m, and the table was placed center in a lab with some clearance of surrounding equipment. Depending on the object-to-be-imaged, the table rotation speed was chosen to prevent aliasing according to (10). A styrofoam head-dummy coated with metallic paint was used in measurements (see Fig. 2b), and it could be measured using  $\Delta\theta = 0.12^\circ$  steps as its diameter was smaller than 30 cm. The angular step was realized by setting the table rotation to a speed of  $1.2^\circ/\text{s}$  and the number of collected sweeps was  $M = 2998$  to cover a full  $360^\circ$  in this particular case. This equates to about 5 minutes of continuous measurement.

In Fig. 2a an ISAR image of the head-dummy is shown (nose is facing south-east). A circularly symmetric median filter of diameter 1.5 cm is applied to all produced images in order to smooth them. Also, images apply large collection angles and should therefore not be regarded as accurate estimates of the RCS distribution, but rather as a "reflection intensity" image. Accordingly, the images are normalized and

displayed in decibels relative to the max value (dBmax). Fig. 2a captures the head contours and it is possible to distinguish some major reflection points on a 1-2 cm scale. Notably, we see an inner ring which is most likely due to reflections off the neck. This is a consequence of the 2D-geometry formulation of the imaging algorithm, and energy contained in different elevation planes will be superposed as demonstrated by Fig. 2a.

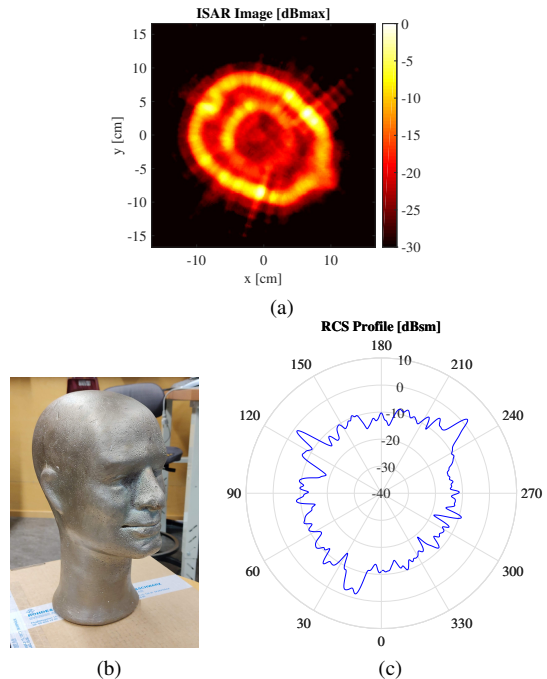


Fig. 2. (a): ISAR image of head-dummy. (b): Picture of head-dummy. (c): RCS profile of head-dummy.

The RCS profile in Fig. 2c is a polar plot with respect to the viewing angle of range-gated data processed according to (3) with  $f = 243$  GHz. Such data is smoothed in the angular dimension to maintain a consistent  $2^\circ$  angular resolution, and is presented in decibels square meter (dBsm). As discussed in section III-A, this is the integrated RCS over the illuminated region. Comparing Fig. 2a and 2c and acknowledging that they are produced from the same data set, one can see that the integrated RCS reaches its largest values as the radar is facing the strongest reflection points head-on (the orientation is exactly the same). Apparently, the relatively flat area around the temples or ears produce strong specular reflections.

Next, measurements of a steering wheel are presented in Fig. 3. This time, sweeps are only recorded for a total of  $180^\circ$ . The steering wheel was placed upright as illustrated in Fig. 3b on the table facing away from the radar by approximately  $90^\circ$  at the start. This way, the entire front of the steering wheel is scanned and a maximum is seen in Fig. 3c of around  $-5$  dBsm when it is facing the radar head-on. In Fig. 3a the contours of the left-facing steering wheel can be seen. The front shows strong specular reflections in agreement with the RCS profile, but there is a slightly curved shape of considerable energy on

the back-side (to the right in the image). These reflection points are most likely due to a metallic component of the steering wheel mount inside the plastic cover. The image thus illustrates an example of the penetrative capabilities of sub-THz radiation in the case of plastics.

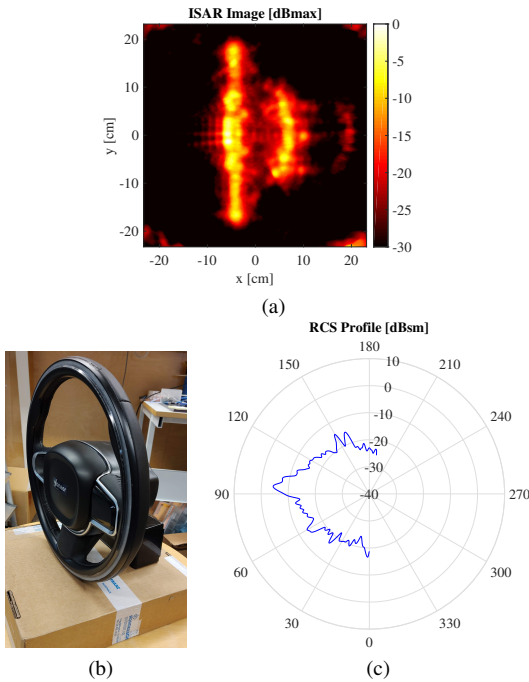


Fig. 3. (a): Steering wheel ISAR image. (b): Picture of steering wheel. (c): RCS profile of steering wheel.

As illustrated by the above presented measurements, ISAR images prove a powerful tool in object radar characterization as it reveals information related to various geometries and materials. Such images can play an important role in the development of the full radar-car cabin interaction/system, but are less telling of direct radar parameters, such as the radar received power, compared to the RCS profiles.

Lastly, RCS profiles of two different human subjects are shown in Fig. 4.

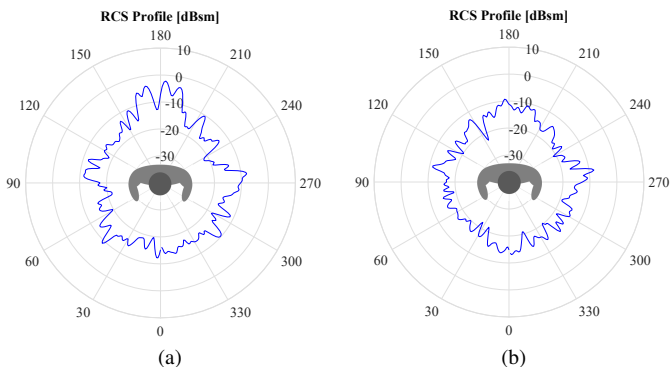


Fig. 4. (a): RCS profile of human subject. (b): RCS profile of another human subject.

The radar was placed in level with the chest area in both cases and the subjects are seated. No ISAR images are provided in this case, as such attempts gave unintelligible results. This was probably due to the fact that a human subject might move during the long collection interval whilst ISAR requires perfectly stationary targets. Another possibility is that the human subject’s breathing pattern results in relatively fast chest movements and causes aliasing. An illustration of a human target (top-view) is provided to show the subjects’ approximate orientation, which is with the chest facing the the 0° mark on the polar axis. In both cases, the human RCS is around  $-15$  dBsm when illuminated from the front.

## V. CONCLUSION

A compact system for measuring RCS at a frequency of 243 GHz has been developed and used to characterize various targets present in a typical car cabin. A few of the results are presented here. It utilizes two complementary analysis methods which can be analysed jointly to give detailed and intuitive view of in-cabin objects’ reflective properties. This was done by examining both the integrated and distributed RCS via RCS profiles and ISAR images, respectively. The effects of peripheral scatterers and multipath are avoided through the use of range-domain processing in both cases. The high-resolution capabilities of the sub-THz spectrum has also been demonstrated, as individual reflection points can be distinguished on a centimeter scale in produced ISAR images.

## ACKNOWLEDGMENT

This project has received funding from the European Union’s Horizon 2020 research and innovation programme under grant agreement No. 824962. We would like to thank the Car2TERA project consortium members and reviewers for encouraging words and valuable input. We are thankful for the many technical discussions with Olof Eriksson, Hans Herbertsson and Zhongxia Simon He who have helped shape the RCS measurement system. Thank you to Viet Lê for getting us up to speed on his measurements, and showing us how to control the VNA with Python. Lastly, a big thank you to John, Johan and Daniel of the Veoneer Concepts and Validation-team for putting together the rotating table.

## REFERENCES

- [1] N. A. Abbasi, A. F. Molisch, and J. C. Zhang, “Measurement of directionally resolved radar cross section of human body for 140 and 220 ghz bands,” in *2020 IEEE Wireless Communications and Networking Conference Workshops (WCNCW)*, 2020, pp. 1–4.
- [2] R. J. Sullivan, *Radar Foundations for Imaging and Advanced Concepts*. Raleigh NC: SciTech Publishing Inc., 2004, ch. 1.
- [3] —, *Radar Foundations for Imaging and Advanced Concepts*. Raleigh NC: SciTech Publishing Inc., 2004, ch. 6.
- [4] —, *Radar Foundations for Imaging and Advanced Concepts*. Raleigh NC: SciTech Publishing Inc., 2004, ch. 3.
- [5] Y. Ding and D. Munson, “A fast back-projection algorithm for bistatic sar imaging,” in *Proceedings. International Conference on Image Processing*, vol. 2, 2002, pp. II–II.
- [6] D. Mensa, S. Halevy, and G. Wade, “Coherent doppler tomography for microwave imaging,” *Proceedings of the IEEE*, vol. 71, no. 2, pp. 254–261, 1983.